Phase Selection and Structure of Low-Defect-Density γ-Al_2O_3 Created by Epitaxial Crystallization of Amorphous Al_2O_3

Rui Liu[a,*], Omar Elleuch[b], Zhongyi Wan[c], Peng Zuo[a], Tesia D. Janicki[c], Adam D. Alfieri[a], Susan E. Babcock[a], Donald E. Savage[a], J. R. Schmidt[c], Paul G. Evans[a], and Thomas F. Kuech[b]

[a] *Department of Materials Science and Engineering, University of Wisconsin-Madison, Madison, WI 53706, United States*

[b] *Department of Chemical and Biological Engineering, University of Wisconsin-Madison, Madison, WI 53706, United States*

[c] *Department of Chemistry, University of Wisconsin-Madison, Madison, WI 53706, United States*

Keywords: Al_2O_3, Solid phase epitaxy, Polymorphism, Phase selection, Thin-film heterostructures, Thin-film defects

Abstract

A multi-step phase sequence following the crystallization of amorphous Al_2O_3 via solid-phase epitaxy (SPE) points to methods to create low-defect density thin films of the metastable cubic γ-Al_2O_3 polymorph. An amorphous Al_2O_3 thin film on a (0001) α-Al_2O_3 sapphire substrate initially transforms upon heating to form epitaxial γ-Al_2O_3, followed by a transformation to monoclinic θ-Al_2O_3, and eventually to α-Al_2O_3. Epitaxial γ-Al_2O_3 layers with low mosaic widths in x-ray rocking curves can be formed via SPE by crystallizing the γ-Al_2O_3 phase from amorphous Al_2O_3 and avoiding the microstructural inhomogeneity arising from the spatially inhomogeneous transformation to θ-Al_2O_3. A complementary molecular dynamics (MD) simulation indicates that

the amorphous layer and γ-Al_2O_3 have similar Al coordination geometry, suggesting that γ-Al_2O_3 forms in part because it involves the minimum rearrangement of the initially amorphous configuration. The lattice parameters of γ-Al_2O_3 are consistent with a structure in which the majority of the Al vacancies in the spinel structure occupy sites with tetrahedral coordination, consistent with the MD results. The formation of Al vacancies at tetrahedral spinel sites in epitaxial γ-Al_2O_3 can minimize the epitaxial elastic deformation of γ-Al_2O_3 during crystallization.

1. Introduction

Polymorphism is a widespread phenomenon in metal oxides due to the similarity of valence, bonding configuration, and density among phases with different structures but identical compositions.[1] The phenomenon occurs in a wide range of materials and can arise in part from the complexity that accompanies the creation of compounds involving several metal ion species. Even comparatively chemically simple oxides consisting of a single metal ion, however, can have several metastable crystal structures with corresponding differences in density, symmetry, and ionic coordination. These polymorphs can exhibit significant differences in properties relevant to their direct use in optical, electronic, magnetic, and catalytic applications their indirect application as substrates for epitaxial growth of other compounds.[2-5] The existence of multiple polymorphs leads to a range of kinetic phenomena in crystallization, especially in nanoscale systems in which the structure is influenced by the proximity of surfaces and interfaces, and by complex elastic stress distributions.[3, 4, 6, 7]

The synthesis of phase-pure metastable oxides, especially in the form of thin films, has been challenging because in the best cases the polymorphs exhibit only small differences in free energy with respect to the stable phase or other competing metastable phases.[8-13] Conditions that favor the thermodynamically stable phase, such as high temperatures and long annealing times, can make the metastable polymorphs highly unfavorable and thus can make their formation even more challenging. Synthesis methods designed to yield metastable polymorphs of a selected compound thus often yield materials in which multiple polymorphs are present. The practical implications of this synthesis challenge are that it is particularly difficult to produce metastable polymorphs with the degree of control required to employ their promising properties in applications and to conduct and to interpret experiments to determine their structure and properties.

For example, a mixture of epitaxial anatase and brookite grains are formed during epitaxial growth of TiO_2 on (100)-oriented yttria-stabilized zirconia (YSZ).[13] The formation of these phase mixtures hinders the understanding of the physical properties of all of the polymorphs and of the phase transformations between polymorphs.[8] Advances in the fundamental understanding of polymorph selection promise to allow particular metastable phases to be formed more precisely. For example, the selection of an appropriate substrate may promote the formation of a particular polymorph.[8, 9, 12, 13] Substrates can be selected to stabilize particular polymorphs using first principle calculations, an approach that has been demonstrated with VO_2.[14] A range of parameters beyond elastic mismatch and interfacial bonding, however, contribute to the determination of the polymorph arising during crystallization and additional approaches to polymorph selection are both possible and valuable. We report methods through which a detailed study of the kinetics of epitaxy and transitions between metastable phases can be employed to yield improved control over the formation of metastable γ-Al_2O_3 and a drastically reduced density of structural defects.

Epitaxial crystallization from amorphous precursors allows the synthesis of crystalline oxides while controlling the selection and sequence of polymorphs. Crystallization from the amorphous form with an orientation or phase selected using a seed crystal is termed solid phase epitaxy (SPE).[15] The crystallization and phase transformation occur through the atomic reconfiguration at interfaces. There are indications that the polymorph selection can be guided by interfacial and chemical effects. For example, polycrystalline pre-deposited Cr_2O_3 layers can be used to select the rhombohedral corundum form of Al_2O_3, α-Al_2O_3.[16]

Aluminum oxide, Al_2O_3, exhibits multiple polymorphs and has widespread applications in electronic materials, catalysis, and surface passivation.[17-19] The polymorphs of Al_2O_3 include the thermodynamically stable phase at ambient pressure, α-Al_2O_3, as well as several structural phases that are metastable at atmospheric pressure.[20-22] Among these metastable phases are monoclinic θ-Al_2O_3, cubic γ-Al_2O_3, and tetragonal δ-Al_2O_3.[2, 23, 24] Transformations between the polymorphs of Al_2O_3 can occur over relatively long periods of time, approximately equal to the duration of practical experiments, and thus several phases observed simultaneously in experiments. The Al_2O_3 polymorphs have several sets of planes with interplanar spacings that are within the resolution of commonly employed x-ray diffraction techniques, which makes it difficult to obtain a precise solution of the structures from powders with high defect densities.[2]

The initial crystallization of amorphous Al_2O_3 often occurs through the formation of γ-Al_2O_3.[2, 25-32] As we show below, the geometric arrangement of ions in amorphous Al_2O_3 has a greater similarity to γ-Al_2O_3 than to other polymorphs. Planar thin films of amorphous Al_2O_3 on Al_2O_3 crystallize into γ-Al_2O_3 upon heating and subsequently convert to the α-Al_2O_3 at high temperature.[29, 30, 33-39] There are indications that the sequence of phases in the crystallization of Al_2O_3 is different in nanoscale geometries. For example, lateral crystallization of Al_2O_3 from α-Al_2O_3 seeds results in the formation of α-Al_2O_3 directly, with minimal formation of γ-Al_2O_3.[40]

SPE of Al_2O_3 on sapphire substrates has previously been studied using amorphous Al_2O_3 created by methods including electron-beam evaporation, ion implantation, and atomic layer deposition (ALD).[29, 34-39] SPE leads to the formation of γ-Al_2O_3 from the amorphous layers, which occurs with a rate matching the duration of practical experiments for temperatures above approximately 700 °C.[29, 34, 37] The γ-Al_2O_3 then transforms to the stable α-phase at higher temperature, often above 800 °C.[29, 34, 37] Here we present structural evidence that an intermediate θ-Al_2O_3 phase forms during this transformation, which has important consequences for the microstructure and potential application of γ-Al_2O_3 thin films.

The experiments and simulations reported here include detailed structural characterization and molecular dynamics (MD) simulations of the initial stages of the crystallization of amorphous Al_2O_3 and the kinetic regimes in which γ-Al_2O_3 and θ-Al_2O_3 are favored. The results reveal that γ-Al_2O_3 can be formed with minimal formation of the competing polymorphs. The initially amorphous Al_2O_3 film on (0001) α-Al_2O_3 substrate is shown schematically in Fig. 1(a). The structures of the crystallized γ-Al_2O_3 and the θ-Al_2O_3 layers formed by the transformation from γ-Al_2O_3 are shown in Figs. 1(b) and (c), respectively. The epitaxial relationships depicted in Fig. 1 are consistent with the experimental results and the structural principles guiding the proposed interface configuration are described below.

The interpretation of the x-ray diffraction results is guided by considering the reciprocal-space locations of the x-ray reflections of γ-Al_2O_3 and θ-Al_2O_3. Figure 1(d) illustrates the reciprocal-space locations of several γ-Al_2O_3 and θ-Al_2O_3 x-ray reflections considered in this manuscript. The diagram in Fig. 1(d) includes reflections for two variants of γ-Al_2O_3 and six structural variants of θ-Al_2O_3, with reciprocal-space locations the experimental observations below. The γ-Al_2O_3 and θ-Al_2O_3 x-ray reflections along the surface-normal direction of reciprocal space are not widely separated. The $20\bar{1}$ reflection of θ-Al_2O_3 and the 111 reflection of γ-Al_2O_3, for example, have interplanar spacings that differ by only 0.05 Å. The small differences make it difficult to distinguish these reflections using measurements of the diffracted intensity along the surface normal, i.e. conventional thin-film x-ray $\theta/2\theta$ scans. Similarly, there are several other strong reflections at which the γ-Al_2O_3 and θ-Al_2O_3 are indistinguishable. These reflections have been studied in previous reports, and as a result, the θ-Al_2O_3 phase has not been reported in studies of the crystallization of amorphous Al_2O_3 on α-Al_2O_3.[29, 34-39] The experiments here employ two sets of reflections in which γ-Al_2O_3 and θ-Al_2O_3 can be separately probed, as illustrated in Fig. 1(d). Reflections in the γ-Al_2O_3 400 family and θ-Al_2O_3 600 family are close together but can be distinguished within the resolution of thin-film x-ray diffraction experiments and the angular width of the reflections of practical samples.

Crystallized Al_2O_3 thin films produced from amorphous layers typically have x-ray rocking curve angular widths that are far larger than single crystals, indicating that there is a comparatively high concentration of defects.[2, 29, 31, 37, 39] The high defect density reduces the usefulness of materials exhibiting multiple phases, for example in applications as substrates for subsequent epitaxial growth. In addition, high-resolution thin-film x-ray diffraction measurements of the lattice parameters and microstructural features are impractical in poorly ordered structures. The results here indicate that the phase transformation between polymorphs and the resulting structural inhomogeneity contribute significantly to this mosaic broadening. The full width at half maximum (FWHM) of the rocking curves of γ-Al_2O_3 222 x-ray reflection under these conditions is 0.03°, indicating low-mosaicity in the film. FWHM value is much smaller than the best value reported in previous studies without such control, 1.4°.[31] The discovery of this phase sequence in epitaxial thin films allows low-defect-density γ-Al_2O_3 to be formed under conditions with a low concentration of θ-Al_2O_3. The large single-crystalline γ-Al_2O_3 can be used as substrates for materials with cubic or hexagonal structures, which can broaden the choices of substrates for oxides and enable large area processing on low-defect-density commercial substrates.

The low angular mosaic width of the x-ray reflections of γ-Al_2O_3 produced during the initial crystallization allows this previously unresolved structural problem to be addressed. For example, determining which sites are the Al vacancies sit in the partially occupied spinel structure in thin films of γ-Al_2O_3 has not been possible due to the high mosaicity of thin films samples and the coexistence of multiple structural phases.[2, 41-43] Al vacancies can sit on sites with either octahedral or tetrahedral coordination.[44] Calculations suggest that the lowest-energy configurations in bulk γ-Al_2O_3 corresponds to a distribution vacancies between tetrahedral and octahedral sites.[45] The lattice parameter of γ-Al_2O_3 varies depending on the locations of Al vacancies due to differences in the Al-O bond length,[27, 28, 45] which indicates that occupation may in turn be affected by elastic stress during synthesis. Even more intriguingly, the variation in the lattice parameter may allow γ-Al_2O_3 to adopt a value of the lattice parameter to minimize the elastic energy. Both experiment and simulation results suggest that Al vacancies at tetrahedral spinel sites in epitaxial γ-Al_2O_3 can minimize the elastic deformation of γ-Al_2O_3.

2. Methods

2.1 Deposition and heating

Amorphous Al_2O_3 films with thicknesses of 100 nm were deposited on (0001) α-Al_2O_3 substrates by ALD. The substrates were prepared by sonication in deionized (DI) water for 40 min and heating to 1400 °C in air for 10 h. These processes yielded a stepped surface morphology with uniform terrace width, as observed using atomic force microscopy. The substrate was cooled to 1000 °C, removed from the furnace, immediately loaded into the ALD reactor under flowing high-purity N_2 gas. Surface preparation before deposition was an important factor in the subsequent crystallization of the Al_2O_3 layers. Amorphous thin films deposited on substrates when there was a significant delay between the introduction to the ALD reactor resulted in poorly ordered crystalline after heating, suggesting that the interfacial contamination between the substrates and the thin films need to be controlled in order to obtain high quality thin films. The ALD reactor was held at 200 °C during the deposition. The ALD process consisted of a series of gas pulses: (i) trimethyl aluminum (in N_2 carrier gas) for 5 s at 0.7 Torr, (ii) N_2 purge for 20 s at 0.5 Torr, (iii) H_2O (in N_2 carrier gas) for 18 s at 1.5 Torr, and (iv) N_2 purge for 30 s at 0.5 Torr. The deposition rate for Al_2O_3 was 1.1 Å/cycle. The amorphous films reported here were obtained with layers deposited using a total of 850 cycles.

The amorphous Al_2O_3 thin films were crystallized and transformed between polymorphs by heating in O_2 gas at atmospheric pressure for 1 h at temperatures from 750 °C to 1020 °C. After heating, the samples were removed from the furnace and cooled in room-temperature air at atmospheric pressure.

2.2 Characterization

A high-resolution diffractometer (Empyrean, Panalytical Inc.) was used for both x-ray reflectivity and high-resolution x-ray diffraction. The incident beam optics employed either a multilayer mirror that yields high-intensity Cu $K\alpha$ radiation or a combination of the multilayer mirror and a channel-cut crystal that yields monochromatic Cu $K\alpha_1$ radiation. A second diffractometer (D8 ADVANCE, Bruker, Inc.) employed a Cu $K\alpha$ point-focus beam and an area x-ray detector was used to determine the polymorph composition and orientation.

2.3 MD simulation methods

Classical MD simulation probed the epitaxial crystallization of amorphous Al_2O_3. The interatomic potential employed in these simulations had previously been calibrated using the experimental lattice parameters of α-Al_2O_3 and the nearest neighbor Al-O distance.[46] The amorphous structure produced using this potential also agrees with x-ray and neutron diffraction observations.[47] The interatomic potentials take the Coulomb-Buckingham form in which the short-range electrostatics, the exponential repulsion, and van del Waals attraction terms are cut off at 8.0 Å. The particle-mesh Ewald method was used to compute the long-range electrostatic interaction.

The MD simulation was conducted using the GROMACS 2018 program.[48] The temperature was set using a stochastic-term-based velocity-rescaling thermostat with a 0.1 ps relaxation time. Amorphous Al_2O_3 at selected temperatures and densities was generated using the following procedure. An α-Al_2O_3 crystal containing 4320 atoms (864 formula units) was first equilibrated at 1600 K at 1 atm using the Berendsen barostat in the isothermal-isobaric ensemble. All simulations after the initial equilibration of α-Al_2O_3 was conducted in the canonical ensemble. After the equilibration, the system was heated to 5000 K and then quenched to 3000 K at a rate of 20 K/ps, which removed the dependence of final amorphous structure on the starting polymorph. The density of the amorphous Al_2O_3 system was changed to 3.0 g/cm^3, approximately matching the experimentally observed density, by rescaling atomic positions and the size of the simulation box along the direction that was subsequently used as the surface normal during simulations of epitaxial crystallization. The simulation box dimensions along the other two directions were not adjusted in order to allow the amorphous structure to be joined to the substrate in a subsequent step. The final amorphous Al_2O_3 was obtained by quenching the system from 3000 K to 1600 K at 2 K/ps and an equilibrating for 200 ps after quenching.

The amorphous-crystalline interface was created by appending the amorphous structure to the (0001) surface of an equilibrated α-Al_2O_3 supercell containing 2160 atoms serving as the substrate for epitaxial crystallization. A vacuum layer with a thickness of 30 Å was added on top of the amorphous structure. A two-step relaxation was employed before production run to remove artifacts in the simulated amorphous/α-Al_2O_3 interface structure. An initial relaxation step was performed in which the α-Al_2O_3 substrate was subjected to a strong position constraint so that only the amorphous layer relaxed. In a second step, all atoms except the ones within 8 Å of the amorphous-crystalline interface were subject to the same position constraint so that atoms near interface were fully relaxed. Both relaxations employed durations of 200 ps at 1600 K.

The production run had a simulated duration of 20 ns. A layer of α-Al_2O_3 with a thickness of 5 Å at the bottom of the simulation box, farthest from the interface, was frozen in order to mimic a semi-infinite substrate. The results below are analyzed using a coordinate system in which the *z*-axis of is along the [0001] direction of the crystalline α-Al_2O_3 substrate.

The results of the MD simulation were studied using a statistical analysis of the coordination of the Al and O atoms. The Steinhardt order parameter $\bar{q}_{l,\beta-\beta}(i)$ was used to distinguish between different polymorphs of Al_2O_3.[49] The quantity $\bar{q}_{l,\beta-\beta}(i)$ was computed by first defining a quantity $q_{lm,\beta-\beta}(i)$ to measure the coordination symmetry up to the first coordination shell:

$$q_{lm,\beta-\beta}(i) = \frac{1}{N_\beta(i)} \sum_{j=1}^{N_\beta(i)} Y_{lm}(\boldsymbol{r}_{ij}) \tag{1}$$

Here the index i enumerates all atoms of type β, $N_\beta(i)$ is the number of nearest neighbors of type β around the atom with index i, and l and m are integer parameters where m runs from $-l$ to l. The functions $Y_{lm}(\boldsymbol{r}_{ij})$ are spherical harmonics and $\boldsymbol{r}_{ij}$ is the unit vector from atom i to atom j. A second quantity, $\bar{q}_{lm,\beta-\beta}(i)$, provides information on the coordination symmetry up to the second coordination shell by averaging of $q_{lm,\beta-\beta}(i)$ over its neighbors of type β:

$$\bar{q}_{lm,\beta-\beta}(i) = \frac{1}{1+N_\beta(i)} \left[q_{lm,\beta-\beta}(i) + \sum_{j=1}^{N_\beta(i)} q_{lm,\beta-\beta}(j) \right] \tag{2}$$

Here the sum includes atom i and its neighbors of type β. Taking the average of $q_{lm,\beta-\beta}(i)$ provides a clearer distinction between different crystal structures at the price of losing coordination information around single atoms. The Steinhardt bond order parameter $\bar{q}_{l,\beta-\beta}(i)$ for atom i is obtained by summing over m, yielding a rotationally invariant result ranging from 0 to 1 that is useful in recognizing the crystal structure regardless of the spatial orientation:

$$\bar{q}_{l,\beta-\beta}(i) = \sqrt{\frac{4\pi}{2l+1}\sum_{m=-l}^{l}\left|\bar{q}_{lm,\beta-\beta}(i)\right|^2} \quad (3)$$

The Steinhardt order parameter is sensitive to different coordination symmetries depending on the choice of l.[50] The oxygen sublattice in the polymorphs of Al_2O_3 discussed in this paper is either hexagonal close packed, as for α-Al_2O_3, or face-centered cubic (FCC), as in γ-Al_2O_3 and θ-Al_2O_3. Both symmetries can be probed by the $l = 6$ spherical harmonics. Hence $\bar{q}_{6,O-O}$ and $\bar{q}_{6,Al-Al}$ were used in this paper to identify different polymorphs of Al_2O_3.

The coordination number distribution of O atoms around Al atoms can be determined by computing the fraction of various Al-O polyhedra in which Al is coordinated with x=3, 4, 5, or 6 O ions. The x=4 and x=6 case correspond to tetrahedral and octahedral coordination, respectively. An O atom is considered as coordinated to the central Al atom if their separation is within a hard cutoff r_c = 2.5 Å, which is the first minimum of the partial radial distribution function between Al atoms and O atoms. In this paper, coordination number distribution of O atoms around Al atoms for simulated amorphous Al_2O_3 and epitaxial γ-Al_2O_3 were computed to determine the distribution of Al atoms over tetrahedral and octahedral spinel sites.

3. Results and Discussion

3.1 Polymorph identification and phase fractions of γ-Al_2O_3 and θ-Al_2O_3

The crystallization of amorphous Al_2O_3 resulted in the development of a sequence of crystalline phases. The mass density, as evaluated using x-ray reflectivity, provided a guideline for the overall progress of the crystallization. The density of the as-deposited amorphous Al_2O_3 layers determined from the critical angle for total external x-ray reflection was 3.1 ± 0.1 g/cm^3. This amorphous layer density matched the value reported in the literature.[51] The crystallization of Al_2O_3 resulted in a decrease of the film thickness and an increase in density, both of which were apparent in x-ray reflectivity measurements. Al_2O_3 layers heated to a comparatively low temperature of 750 °C were not crystallized after 1 h and exhibited decrease in thickness of only 3%, corresponding to a small increase with respect to the as-deposited density. Heating to between 800 °C and 1020 °C for 1h, resulted in a decrease in the thickness by 16% to a density of 3.5 ± 0.1 g/cm^3, consistent with the crystallization of the Al_2O_3 layer. The densities of θ-Al_2O_3 (3.61 g/cm^3) and γ-Al_2O_3 (3.60 g/cm^3) could not be distinguished within the precision of the x-ray reflectivity measurement.[23, 52]

The dependence of phase composition of the Al_2O_3 layer on heating temperature was studied using a series of x-ray diffraction measurements. The x-ray characterization employed a region of reciprocal space in which reflections in the θ-Al_2O_3 600 family and the γ-Al_2O_3 400 family appear and can be clearly distinguished, as illustrated in Fig. 2(a). The intensities $I_{\gamma 400}$ and $I_{\theta 600}$ for the γ-Al_2O_3 400 and θ-Al_2O_3 600 families, respectively, were both obtained by integrating and averaging the intensities of the six orientations of each reflection. The intensities obtained in this way are shown in Fig. 2(b) for layers heated to a series of different temperatures.

A quantitative analysis of the intensities in Fig. 2(b) allows the volume fractions of the γ-Al_2O_3 and θ-Al_2O_3 phases to be determined. With volumes V_γ and V_θ for the two phases, the volume fractions f_γ and f_θ are $f_\gamma = \frac{V_\gamma}{V_\theta + V_\gamma} = \frac{I_{\gamma 400}}{I_{tot,corr}}$ and $f_\theta = \frac{V_\gamma}{V_\theta + V_\gamma} = \frac{cI_{\theta 600}}{I_{tot,corr}}$, with $I_{tot,corr} = I_{\gamma 400} + cI_{\theta 600}$. Here $c = \frac{|F|^2_{\gamma 400}}{|F|^2_{\theta 600}} \frac{LP_{\gamma 400}}{LP_{\theta 600}} \frac{N_{\theta 600}}{N_{\gamma 400}} = 7.69$, where F, with appropriate subscripts, is the structure factor for each set of reflections. LP is Lorentz-polarization factor for the two phases. N is the number of variants that contribute to the integrated intensity: 2 for the γ-Al_2O_3 400 reflections and 6 for θ-Al_2O_3 600 reflections. The volume fractions of γ-Al_2O_3 and θ-Al_2O_3 are shown as a function of temperature in Fig. 2(c).

The intensities of reflections for both phases are zero, within experimental uncertainty, following heating to 750 °C. Two other temperature regimes are apparent in Figs. 2(b) and (c). After heating to 800 and 850 °C the majority of the crystallized layer is in the γ-Al_2O_3 phase, with and f_θ = 30%. Higher temperatures during the heating process, from 900 °C to 1020 °C, resulted in higher values of f_θ, approximately 80% after heating to 1020 °C. Scanning transmission electron microscopy measurements were conducted for film heated to 1020 °C and the results indicated that both γ-Al_2O_3 and θ-Al_2O_3 appeared in the first a few tens of nm from the interface and are approximately randomly distributed in the layer crystallized under these conditions.

A further experiment was conducted to determine whether θ-Al_2O_3 formed directly from amorphous Al_2O_3 or resulted from a transformation from γ-Al_2O_3. An initially amorphous Al_2O_3 layer was heated at 800 °C for 1 h to form γ-Al_2O_3 and then heated again to 1020 °C for a further 1 h. The fraction of θ-Al_2O_3 following this two-step process was 80%, which is to the same as the fraction observed in the film directly heated to 1020 °C for 1 hour. We thus conclude that the θ-Al_2O_3 results from a transformation from the γ-Al_2O_3 rather than a direct crystallization from the amorphous layer into θ-Al_2O_3.

The Steinhardt order parameter $\bar{q}_{6,Al-Al}$ and $\bar{q}_{6,O-O}$ was used to identify the polymorphs of Al_2O_3 formed during crystallization in MD simulations. Reference values of these parameters were obtained from simulations of the bulk phases at 1600 K and 1 atm. The probability distribution of $\bar{q}_{6,Al-Al}$ and $\bar{q}_{6,O-O}$ and their joint distribution for four different Al_2O_3 structures reached after different stages in the MD simulation are shown in Fig. 3(a). The marginal distributions are normalized on the unit interval $[0,1]$ and the joint distributions are normalized on the unit region $[0,1] \times [0,1]$. γ-Al_2O_3 and θ-Al_2O_3 have nearly identical $\bar{q}_{6,O-O}$ distributions with a peak value of 0.32, because the O sublattices in both γ-Al_2O_3 and θ-Al_2O_3 exhibit FCC packing. The most common Al-O coordinations are those in which Al is coordinated with 4 O ions (47%) and 5 O ions (47%). A small proportion, approximately 10%, of the ions are in three-fold and six-fold coordinations. In the epitaxial γ-Al_2O_3 layers produced by the MD simulation the most frequent Al coordinations are tetrahedral coordination (29%) and octahedral coordination (70%). Amorphous Al_2O_3 and γ-Al_2O_3 also have similar distributions of values of $\bar{q}_{6,Al-Al}$ with maxima at 0.12 and 0.15, respectively. The amorphous and γ-Al_2O_3 structures have Al ion arrangements that are more similar to each other as compared to other polymorphs.

The values of the Steinhardt order parameter shown in Fig. 3(a) can be used to interpret the results of the MD simulation. A snapshot of atomic positions and the variation of $\bar{q}_{6,O-O}$ and $\bar{q}_{6,Al-Al}$ as a function of position in MD simulation before crystallization is shown in Fig. 3(b). The α-Al_2O_3 phase shown for the calibration of the Steinhardt order parameter in Fig. 3(a) has a peak value of $\bar{q}_{6,O-O}$ of 0.26 and $\bar{q}_{6,Al-Al}$ of 0.35. The position dependence of $\bar{q}_6(z)$ in Fig. 3 was obtained by averaging of all atoms within from z to $z + 4$ Å. The crystalline region in the simulation (α-Al_2O_3) has values of these parameters of 0.27 and 0.35, as appropriate for the initial conditions of the simulation. The values of $\bar{q}_{6,O-O}$ and $\bar{q}_{6,Al-Al}$ for the amorphous region of Fig. 3(b) are also consistent with the initial expectations.

The phase formed upon crystallization can be determined from the Steinhardt order parameters obtained for the crystallized layers and visual inspection. Figure 3(c) shows a snapshot of the simulation and the spatial variation of $\bar{q}_{6,O-O}$ and $\bar{q}_{6,Al-Al}$ after the completion of crystallization simulation. The expected values of $\bar{q}_{6,O-O}$ and $\bar{q}_{6,Al-Al}$ for the γ-Al_2O_3 phase are 0.32 and 0.15, respectively. The crystallized layer in Fig. 3(c) has values $\bar{q}_{6,O-O}$ and $\bar{q}_{6,Al-Al}$ of 0.31 and 0.15, matching γ-Al_2O_3 closely. These values, however, do not match the θ-Al_2O_3 or α-Al_2O_3 polymorphs, indicating that the MD simulation results in the epitaxial crystallization of γ-

Al_2O_3, consistent with the experiment.

The results shown in Fig. 3 suggest a mechanism for the crystallization of amorphous Al_2O_3. The transformation from amorphous to γ-Al_2O_3 can structurally occur by crystallization of O sublattice into FCC packing with minimal change in the Al atoms arrangement from five-fold coordination to six-fold coordination In this picture, γ-Al_2O_3 forms first out of amorphous Al_2O_3 since the γ-Al_2O_3 polymorphs is structurally more similar to the amorphous structure than θ-Al_2O_3 in terms of Al atom arrangement, which can be seen while comparing the $\bar{q}_{6,Al-Al}$ values in Fig. 3(a).

The formation of the θ-Al_2O_3 in the experiments was studied using a series of x-ray diffraction studies. The crystallographic parameters of the θ-Al_2O_3 phase were probed using the θ-Al_2O_3 $20\bar{2}$ and $40\bar{1}$ families of x-ray reflections, which arise in a region of reciprocal space in which there are no γ-Al_2O_3 reflections. A diagram of the reciprocal space of the θ-Al_2O_3 layers formed in these experiments and the x-ray scattering geometry are shown in Fig. 4(a). The x-ray diffraction patterns acquired as average during a rotation through the Bragg conditions for these reflections after heating to 800 °C and 1020 °C are shown in Figs. 4(b) and (c), respectively. The diffraction patterns were obtained by rotating the sample over 5° range of incident angles with respect to the sample surface. The layer crystallized at 800 °C exhibits only weak reflections of θ-Al_2O_3, which indicates that a small fraction of the film was in the θ-Al_2O_3 phase. Two intense pairs of $20\bar{2}$ and $40\bar{1}$ reflections from two variants of θ-Al_2O_3 were apparent in the film heated at 1020 °C, as shown in Fig. 4(c).

The angular separation of the reflections in Fig. 4(c) was measured using the diffraction angle χ, which is the azimuthal angle between the reflections along the diffraction cone of constant

2θ intercepting the Ewald sphere. The intensities integrated across the regions indicated in the diffraction patterns are shown as a function of χ in Fig. 4(d). The angular separation of the $20\bar{2}$ and $40\bar{1}$ reflections for the layer heated to 1020 °C is 45.7°. The interplanar spacings derived from the values of 2θ and the χ separation in Fig. 4(d) are a=11.9 Å, c=5.62 Å and β=103.3°. The lattice parameter b=2.86 Å by combining these measurements with the measured 2θ angle of the $7\bar{1}\bar{2}$ reflection. The lattice parameters and χ separation are consistent with the reported structure of θ-Al_2O_3.[53] Twelve-fold azimuthal symmetry was observed in the $7\bar{1}\bar{2}$ reflections, which also indicated the phase reached by the transformation from γ-Al_2O_3 is θ-Al_2O_3.

The structural parameters of the γ-Al_2O_3 phase were measured using two sets of x-ray reflections that provided (i) the interplanar spacing along the surface-normal direction of reciprocal space and (ii) the distortion in the plane parallel to the surface. Figure 5(a) shows θ/2θ scans of the films heated to 800 °C and 1020 °C for 1 hour. The thin-film reflections in Fig. 5(a) are indexed with the γ-Al_2O_3 and θ-Al_2O_3 reflections along this line in reciprocal space, which have nearly identical interplanar spacings. As indicated in Fig. 2, films heated to 800 °C, however, consisted mostly of γ-Al_2O_3 and the reflections and the intensity peaks at that temperature can be indexed as the γ-Al_2O_3 111, 222, 333, and, 444 reflections. The (111) interplanar spacing of γ-Al_2O_3 determined from the γ-Al_2O_3 reflections in Fig. 5(a) was 4.53 Å.

An x-ray rocking curve for the γ-Al_2O_3 222 reflection of a sample heated to 800 °C is shown in Fig. 5(b), along with a rocking curve for a layer consisting of a mixture of the γ-Al_2O_3 and θ-Al_2O_3 phases after heating to 1020 °C. The FWHM of the rocking curve of γ-Al_2O_3 is 0.03° after heating at 800 °C. We hypothesize that the larger FWHM of sample heated at 1020 °C arises from the microstructural inhomogeneity associated with the partial transformation from γ-Al_2O_3 to θ-Al_2O_3.

The interplanar spacing of γ-Al_2O_3 in the plane parallel to the surface was measured using the γ-Al_2O_3 400 family of x-ray reflections. Diagrams of the reciprocal space of γ-Al_2O_3 and θ-Al_2O_3 and the x-ray scattering geometry are shown in Fig. 6(a). The schematic in Fig. 6(a) also includes the α-Al_2O_3 $11\bar{2}3$ reflection that serves as a reference for the overall epitaxial relationship. The diffraction patterns in Fig. 6 were obtained by integrating the diffracted intensity while rotating the x-ray incident angle through a range spanning the Bragg conditions of the γ-Al_2O_3 400 and θ-Al_2O_3 600 reflections. The diffraction pattern and integrated intensity as a function of 2θ are shown in Figs. 6(b) and (c) after heating to 800 °C and in Figs. 6(d) and (e) after heating to 1020 °C. The γ-Al_2O_3 (400) interplanar spacing determined from the γ-Al_2O_3 400 reflection was 1.98 Å.

The γ-Al_2O_3 (111) and (400) interplanar spacings are not precisely consistent with cubic symmetry and thus indicate that the γ-Al_2O_3 layer is elastically distorted. Possible sources of elastic distortion include stress remaining after the relaxation of the large epitaxial mismatch between γ-Al_2O_3 and α-Al_2O_3. The hypothetical lattice parameter of undistorted cubic γ-Al_2O_3 can be determined based on the assumption that the remaining strain has biaxial symmetry. The interplanar spacing of a purely in-plane γ-Al_2O_3 $4\bar{2}\bar{2}$ reflection was determined using the difference between the γ-Al_2O_3 222 and 600 reflection vectors. Using the in-plane and out-of-plane interplanar spacings we find that the reflections are fit with a cubic γ-Al_2O_3 phase with lattice parameter 7.88 Å, in-plane strain 0.55%, and out-of-plane strain -0.39%. The calculations employed a Poisson ratio of 0.26 from the literature.[54] Varying the specific choice of the Poisson ratio over the entire reasonable range of possible values does not have a significant impact on the results.

The orientations and contact planes of the epitaxial films were determined from the x-ray diffraction studies. In the θ/2θ scans in Fig. 5(a), γ-Al_2O_3 111 and θ-Al_2O_3 $20\bar{1}$ reflections appear along the normal direction of α-Al_2O_3 (0001) substrate, which indicates that the epitaxial relationship is such that the following planes are parallel: α (0001) || γ (111) || θ $(20\bar{1})$. The asymmetric reflections of γ-Al_2O_3 400 and θ-Al_2O_3 600 appear in the same azimuthal angle with the same sample tilting as the $11\bar{2}3$ reflection of α-Al_2O_3 substrate as shown in Fig. 6(d). The following in-plane directions are thus parallel: α $[1\bar{1}00]$ || γ $[0\bar{1}1]$ || θ [010]. The epitaxial relationship and the bonding configuration at the interfaces between the crystallized γ-Al_2O_3 and θ-Al_2O_3 layers and the α-Al_2O_3 substrate are schematically shown in Figs. 7(a) and (b), respectively. Al atoms at tetrahedral and octahedral sites are colored differently to emphasize the bonding structures and the epitaxial relationships at the interfaces of two phases. The drawings are constructed based on the assumption that the oxygen sublattices are matched at the interfaces.

The azimuthal arrangement of the γ-Al_2O_3 reflections indicates that γ-Al_2O_3 layer forms with two structural variants. In general, rotation around the [111] direction of a cubic crystal should yield reflections with three-fold azimuthal symmetry. Azimuthal rotation of the films produced by SPE, however reveals six intensity maxima, which indicates that two domains are present in the γ-Al_2O_3 layer. The two domains are related by a 180° rotation around [111], which is consistent with the two possible ways that the FCC stacking sequence of the oxygen layers can be continued from the α-Al_2O_3 substrate into the γ-Al_2O_3 layer.

3.2 Sites of Al vacancies in γ-Al_2O_3 and variation of the γ-Al_2O_3 lattice parameter

The conventional unit cell of the spinel structure on which γ-Al_2O_3 is based includes 32 oxygen-ion sites and 24 sites for cations, consisting of 16 sites with octahedral symmetry and 8 with tetrahedral symmetry. The Al_2O_3 composition requires that each conventional unit cell includes only $64/3 \approx 21.33$ Al cations sties and that the remaining $8/3 \approx 2.67$ cation sites be vacant.[27]

The hypothetical structures in which Al vacancies occupy only octahedral sites or only tetrahedral sites are shown in Figs. 8(a) and (b), respectively.

The lattice parameter of γ-Al_2O_3 varies depending on the sites of Al vacancies. The lattice parameter γ-Al_2O_3 determined from the X-ray analysis can thus be used to determine the sites of Al vacancies. The γ-Al_2O_3 lattice parameter ranges from 7.84 Å when Al vacancies are at tetrahedral sites to 7.95 Å when Al vacancies are at octahedral sites.[55, 56] A linear interpolation between these cases indicates that the experimentally observed lattice parameter arises when 64% of the Al vacancies sit on sites with tetrahedral coordination. An example of a distribution of vacancies producing a lattice parameter matching the experimentally observed value is shown in Fig. 8(c). Five of the eight of the Al vacancies in Fig. 8(c) are at tetrahedral sites, close to the value of 64% matching the experimental lattice parameter.

The structure produced by the MD simulation also provides insight into the positions of Al vacancies within the partially occupied spinel unit cell. The coordination number distribution of epitaxial γ-Al_2O_3 was computed using positions obtained in a 100 ps MD relaxation of structures incorporating only octahedral or only tetrahedral vacancy sites. When the vacancies are only at octahedral sites, the percentage of Al atoms with octahedral coordination is 62.5%. With vacancies only at tetrahedral sites, the same percentage is 75%. The percentage of Al atoms with octahedral coordination for the epitaxial γ-Al_2O_3 produced by MD simulation is 70%, which implies that 78% of the vacancies are at tetrahedral sites by comparing to the two extreme percentages of the occupation sites.

The variation of the lattice parameter of the γ-Al_2O_3 leads to the intriguing possibility that the distribution of vacancy sites is adopted during epitaxy to select a lattice parameter that minimizes the elastic energy. The γ-Al_2O_3 on α-Al_2O_3 selects a configuration in the structural mismatch between epitaxial γ-Al_2O_3 and substrate α-Al_2O_3 is reduced by favoring the vacancies on tetrahedral sites.

4. Conclusions

Amorphous Al_2O_3 films deposited on (0001) α-Al_2O_3 sapphire substrates initially transform upon heating to form epitaxial γ-Al_2O_3, followed by a transformation to a metastable monoclinic θ-Al_2O_3, and eventually to α-Al_2O_3. The MD simulation results demonstrated that the γ-Al_2O_3 directly formed from the amorphous films because Al coordination geometry better match those of amorphous film compared with other polymorphs. The low mosaicity allows us to identify the distribution of Al vacancies in the partially occupied spinal structure of γ-Al_2O_3 by strain analysis. The measured lattice parameters of the relaxed γ-Al_2O_3 indicate that 64% of the Al vacancies sit on sites with tetrahedral coordination in the γ-Al_2O_3 thin film selected by SPE. Statistical analysis of the simulated γ-Al_2O_3 indicated that 78% of the Al vacancies sit on sites with tetrahedral coordination. Both the experiment and simulation results indicate that more of the Al vacancies occurred on sites with tetrahedral coordination to minimize the elastic deformation of γ-Al_2O_3.

The crystallization of γ-Al_2O_3 with low defect densities by a kinetic route avoiding the transformation to θ-Al_2O_3 raises several intriguing possibilities. The single crystal γ-Al_2O_3 is a potential substrate candidate for thin films with cubic or hexagonal structures, which can broaden the choices of the lattice parameters of the substrates for oxides and enable large area processing on low-defect density commercial substrates. The θ-Al_2O_3 polymorph observed here resulted from a transformation from γ-Al_2O_3, rather than a direct crystallization from the amorphous form into θ-Al_2O_3 directly. As a result, the transformation to θ-Al_2O_3 resulted in a significant broadening of the initially narrow mosaic width of the γ-Al_2O_3 reflections.

More generally, oxide SPE can enable and select metastable polymorphs in epitaxial Al_2O_3 thin films, leading to the possibility that such phases can be included in intricate three-dimensional structures. The crystallization of amorphous Al_2O_3 within hollow crystalline domes with nanoscale wall thicknesses has recently been demonstrated, for example.[57] The selection of specific metastable phases during SPE can broaden the scope of properties available in these geometries.

Acknowledgments

This research was primarily supported by the NSF Division of Materials Research through the University of Wisconsin Materials Research Science and Engineering Center (grant DMR-1720415).

References

1. Sood, S.; Gouma, P. Polymorphic Phase Transitions in Nanocrystalline Binary Metal Oxides. *J. Am. Ceram. Soc.* **2013,** *96*, 351-354.

2. Levin, I.; Brandon, D. Metastable Alumina Polymorphs Crystal Structures and Transition Sequences. *J. Am. Ceram. Soc.* **1998,** *81*, 1995-2012.

3. Zhang, M.; Chen, T.; Wang, Y. Insights into TiO_2 Polymorphs: Highly Selective Synthesis, Phase Transition, and Their Polymorph-Dependent Properties. *RSC Adv.* **2017,** *7*, 52755-52761.

4. Hong, B.; Zhao, J.; Hu, K.; Yang, Y.; Luo, Z.; Li, X.; Gao, C. Facile Synthesis of Various Epitaxial and Textured Polymorphs of Vanadium Oxide Thin Films on the (0006)-Surface of Sapphire Substrates. *RSC Adv.* **2017,** *7*, 22341-22346.

5. Aykol, M.; Dwaraknath, S. S.; Sun, W.; Persson, K. A. Thermodynamic Limit for Synthesis of Metastable Inorganic Materials. *Science Adv.* **2018,** *4*, eaaq0148.

6. Trunov, M. A.; Schoenitz, M.; Dreizin, E. L. Effect of Polymorphic Phase Transformations in Alumina Layer on Ignition of Aluminium Particles. *Combust. Theor. Model.* **2006,** *10*, 603-623.

7. Modeshia, D. R.; Darton, R. J.; Ashbrook, S. E.; Walton, R. I. Control of Polymorphism in $NaNbO_3$ by Hydrothermal Synthesis. *Chem. Comm.* **2009**, 68-70.

8. Lee, S.; Ivanov, I. N.; Keum, J. K.; Lee, H. N. Epitaxial Stabilization and Phase Instability of VO_2 Polymorphs. *Sci. Rep.* **2016,** *6*, 19621.

9. Wang, W. B.; Zhao, J.; Wang, W. B.; Gai, Z.; Balke, N.; Chi, M. F.; Lee, H. N.; Tian, W.; Zhu, L. Y.; Cheng, X. M.; Keavney, D. J.; Yi, J. Y.; Ward, T. Z.; Snijders, P. C.; Christen, H. M.; Wu, W. D.; Shen, J.; Xu, X. S. Room-Temperature Multiferroic Hexagonal $LuFeO_3$ Films. *Phys Rev Lett* **2013,** *110*.

10. Jeen, H.; Choi, W. S.; Biegalski, M. D.; Folkman, C. M.; Tung, I. C.; Fong, D. D.; Freeland, J. W.; Shin, D.; Ohta, H.; Chisholm, M. F.; Lee, H. N. Reversible Redox Reactions in an Epitaxially Stabilized $SrCoO_x$ Oxygen Sponge. *Nat Mater* **2013,** *12*, 1057-1063.

11. Choi, W. S.; Rouleau, C. M.; Seo, S. S. A.; Luo, Z. L.; Zhou, H.; Fister, T. T.; Eastman, J. A.; Fuoss, P. H.; Fong, D. D.; Tischler, J. Z.; Eres, G.; Chisholm, M. F.; Lee, H. N. Atomic Layer Engineering of Perovskite Oxides for Chemically Sharp Heterointerfaces. *Adv Mater* **2012,** *24*, 6423-6428.

12. Schlom, D. G.; Chen, L. Q.; Eom, C. B.; Rabe, K. M.; Streiffer, S. K.; Triscone, J. M. Strain Tuning of Ferroelectric Thin Films. *Annu Rev Mater Res* **2007,** *37*, 589-626.

13. Lotnyk, A.; Senz, S.; Hesse, D. Epitaxial Growth of TiO2 Thin Films on SrTiO3, LaAlO3 and Yttria-Stabilized Zirconia Substrates by Electron Beam Evaporation. *Thin Solid Films* **2007,** *515*, 3439-3447.

14. Ding, H.; Dwaraknath, S. S.; Garten, L.; Ndione, P.; Ginley, D.; Persson, K. A. Computational Approach for Epitaxial Polymorph Stabilization through Substrate Selection. *ACS Appl. Mater. Interfaces* **2016,** *8*, 13086-13093.

15. Evans, P. G.; Chen, Y.; Tilka, J. A.; Babcock, S. E.; Kuech, T. F. Crystallization of Amorphous Complex Oxides: New Geometries and New Compositions via Solid Phase Epitaxy. *Curr. Opin. Solid State Mater. Sci.* **2018,** *22*, 229-242.

16. Jin, P.; Nakao, S.; Wang, S. X.; Wang, L. M. Localized Epitaxial Growth of α-Al_2O_3 Thin Films on Cr_2O_3 Template by Sputter Deposition at Low Substrate Temperature. *Appl. Phys. Lett.* **2003,** *82*, 1024-1026.

17. Nie, X.; Meletis, E. I.; Jiang, J. C.; Leyland, A.; Yerokhin, A. L.; Matthews, A. Abrasive Wear/Corrosion Properties and TEM Analysis of Al_2O_3 Coatings Fabricated using Plasma Electrolysis. *Surf. Coatings Technol.* **2002,** *149*, 245-251.

18. Xu, C.; Goodman, D. W., Ultrathin Oxide Films: Model Catalyst Supports. In *Handbook of Heterogeneous Catalysis*, Ertl, G.; Knözinger, H.; Weitkamp, J., Eds. VCH Verlagsgesellschaft Weinheim, 1997.

19. Collongues, R.; Gourier, D.; Kahn, A.; Boilot, J. P.; Colomban, P.; Wicker, A. β Alumina, A Typical Solid Electrolyte: Latest Developments in Fundamental Approach and in Battery Utilization. *J. Phys. Chem. Solids* **1984,** *45*, 981-1013.

20. O'Dell, L. A.; Savin, S. L. P.; Chadwick, A. V.; Smith, M. E. A ^{27}Al MAS NMR

Study of A Sol–gel Produced Alumina: Identification of the NMR Parameters of the θ-Al_2O_3 Transition Alumina Phase. *Solid State Nucl. Magnet. Resonan.* **2007,** *31*, 169-173.

21. Barker, A. S. Infrared Lattice Vibrations and Dielectric Dispersion in Corundum. *Phys. Rev.* **1963,** *132*, 1474-1481.

22. Newnham, R. E.; de Haan, Y. M. Refinement of the α Al2O3, Ti2O3, V2O3 and Cr2O3 Structures. *Z. Krisltallogr.* **1962,** *117*, 235-237.

23. Krokidis, X.; Raybaud, P.; Gobichon, A.-E.; Rebours, B.; Euzen, P.; Toulhoat, H. Theoretical Study of the Dehydration Process of Boehmite to γ-Alumina. *J. Phys. Chem. B* **2001,** *105*, 5121-5130.

24. Aykol, M.; Persson, K. A. Oxidation Protection with Amorphous Surface Oxides: Thermodynamic Insights from *Ab Initio* Simulations on Aluminum. *ACS Appl. Mater. Interfaces* **2018,** *10*, 3039-3045.

25. Smrcok, L.; Langer, V.; Krestan, J. Gamma-Alumina: A Single-Crystal X-ray Diffraction Study. *Acta Cryst. C* **2006,** *62*, 83-84.

26. Trunov, M. A.; Schoenitz, M.; Zhu, X.; Dreizin, E. L. Effect of Polymorphic Phase Transformations in Al_2O_3 Film on Oxidation Kinetics of Aluminum Powders. *Combust. Flame* **2005,** *140*, 310-318.

27. Cai, S.-H.; Rashkeev, S. N.; Pantelides, S. T.; Sohlberg, K. Phase Transformation Mechanism between γ- and θ-Alumina. *Phys. Rev. B* **2003,** *67*, 224104.

28. Cai, S. H.; Rashkeev, S. N.; Pantelides, S. T.; Sohlberg, K. Atomic Scale Mechanism of the Transformation of Gamma-Alumina to Theta-Alumina. *Phys Rev Lett* **2002,** *89*, 235501.

29. Simpson, T. W.; Wen, Q.; Yu, N.; Clarke, D. R. Kinetics of the Amorphous Gamma Alpha Transformations in Aluminum Oxide: effect of crystallographic orientation. *J. Am. Ceram. Soc.* **1998,** *81*, 61-66.

30. Levin, I.; Bendersky, L. A.; Brandon, D. G.; Ruhle, M. Cubic to Monoclinic Phase Transformations in Alumina. *Acta Mater.* **1997,** *45*, 3659-3669.

31. Yu, N.; McIntyre, P. C.; Nastasi, M.; Sickafus, K. E. High-Quality Epitaxial Growth of Gamma -Alumina Films on Alpha -Alumina Sapphire Induced by Ion-beam Bombardment. *Phys. Rev. B* **1995,** *52*, 17518-17522.

32. Wilson, S. Phase Transformations and Development of Microstructure in Boehmite-Derived Transition Aluminas. *Proc. Brit. Ceram. Soc.* **1979,** *28*, 281-294.

33. McCallum, J. C.; Simpson, T. W.; Mitchell, I. V. Time Resolved Reflectivity Measurements of the Amorphous-to-Gamma and Gamma-to-Alpha Phase Transitions in Ion Implanted Al_2O_3 *Nucl. Instr. Meth. Phys. Res. B* **1994,** *91*, 60-62.

34. Jang, J.; Lee, S. Y.; Park, H.; Yoon, S.; Park, G. S.; Lee, G. D.; Park, Y.; Kim, M.; Yoon, E. Solid-Phase Epitaxial Growth of an Alumina Layer Having a Stacking-Mismatched Domain Structure of the Intermediate Gamma-Phase. *ACS Appl. Mater. Interfaces* **2018,** *10*, 41487-41496.

35. Clarke, D. R. Epitaxial Phase Transformations in Aluminum Oxide. *Phys Status Solidi A* **1998,** *166*, 183-196.

36. Yu, N.; Simpson, T. W.; Mcintyre, P. C.; Nastasi, M.; Mitchell, I. V. Doping Effects on the Kinetics of Solid-Phase Epitaxial-Growth of Amorphous Alumina Thin-Films on Sapphire. *Appl. Phys. Lett.* **1995,** *67*, 924-926.

37. McCallum, J. C.; Simpson, T. W.; Mitchell, I. V. Time Resolved Reflectivity Measurements of the Amorphous-to-Gamma and Gamma-to-Alpha Phase Transitions in Ion Implanted Al2O3. *Nucl. Instr. and Meth. in Phys. B* **1994,** *91*, 60-62.

38. Sklad, P. S.; Mccallum, J. C.; Mchargue, C. J.; White, C. W. The Amorphous-to-Gamma Transformation in Ion-Implanted Al_2O_3. *Nucl Instrum Meth B* **1990,** *46*, 102-106.

39. White, C. W.; Boatner, L. A.; Sklad, P. S.; McCallum, C. J.; J., R.; Farlow, G. C.; Aziz, M. J. Ion Implantation and Annealing of Crystalline Oxides and Ceramic Materials. *Nucl. Instr. and Meth. in Phys. Res. B* **1988,** *32*, 11-22.

40. Maret, H.; Weisberg, D.; Chan, H. M.; Strandwitz, N. C. Seeded Solid-Phase Epitaxy of Atomic Layer Deposited Aluminum Oxide. *Cryst. Growth Des.* **2016,** *16*, 1662-1666.

41. Ernst, F.; Pirouz, P.; Heuer, A. HRTEM Study of A Cu/Al_2O_3 Interface. *Phil. Mag. A* **1991,** *63*, 259-277.

42. John, C.; Alma, N.; Hays, G. Characterization of Transitional Alumina by Solid-State Magic Angle Spinning Aluminium NMR. *Appl. Catal.* **1983,** *6*, 341-346.

43. Shirasuka, K.; Yanagida, H.; Yamaguchi, G.; Kyokaishi, Y. The Preparation of Eta Alumina and its Structure. *J. Am. Ceram. Soc.* **1976,** *84*, 610-613.

44. Mo, S. D.; Xu, Y. N.; Ching, W. Y. Electronic and Structural Properties of Bulk γ -Al_2O_3. *J. Am. Ceram. Soc.* **1997,** *80*, 1193-1197.

45. Maglia, F.; Gennari, S.; Buscaglia, V. Energetics of Aluminum Vacancies and Incorporation of Foreign Trivalent Ions in γ-Al_2O_3: An Atomistic Simulation Study. *J. Am. Ceram. Soc.* **2007,** *91*, 283-290.

46. Matsui, M. A Transferable Interatomic Potential Model for Crystals and Melts in the System CaO-MgO-Al_2O_3-SiO_2. *Mineralog. Mag.* **1994,** *58*, 571-572.

47. Gutiérrez, G.; Johansson, B. Molecular Dynamics Study of Structural Properties of Amorphous Al_2O_3. *Phys. Rev. B* **2002,** *65*, 104202.

48. Berendsen, H. J.; van der Spoel, D.; van Drunen, R. GROMACS: A Message-Passing Parallel Molecular Dynamics Implementation. *Comp. Phys. Commun.* **1995,** *91*, 43-56.

49. Lechner, W.; Dellago, C. Accurate Determination of Crystal Structures based on Averaged Local Bond Order Parameters. *J. Chem. Phys.* **2008,** *129*, 114707.

50. Steinhardt, P. J.; Nelson, D. R.; Ronchetti, M. Bond-Orientational Order in Liquids and Glasses. *Phys. Rev. B* **1983,** *28*, 784-805.

51. Groner, M.; Fabreguette, F.; Elam, J.; George, S. Low-Temperature Al_2O_3 Atomic Layer Deposition. *Chem. Mater.* **2004,** *16*, 639-645.

52. Husson, E.; Repelin, Y. Structural Studies of Transition Aluminas. Theta Alumina. *Europ. J. Solid State. Inorgan. Chem.* **1996,** *33*, 1223-1231.

53. Guse, W.; Saalfeld, H. X-ray Characterization and Structure Refinement of A New Cubic Alumina Phase (σ-Al_2O_3) with Spinel-Type Structure. *N. Jahrbuch Mineral. Monat.* **1990**, 217-226.

54. Tu, B.; Wang, H.; Liu, X.; Wang, W.; Fu, Z. First-Principles Insight into the Composition-Dependent Structure and Properties of γ-Alon. *J. Am. Ceram. Soc.* **2014,** *97*, 2996-3003.

55. Eberhart, J.-P. Etude Des Transformations du Mica Muscovite par Chauffage Entre

700 et 1200 C. *Bull. Minéral.* **1963,** *86*, 213-251.

56. Zhou, R.-S.; Snyder, R. L. Structures and Transformation Mechanisms of the η, γ and θ Transition Aluminas. *Acta Cryst. B* **1991,** *47*, 617-630.

57. Jang, J.; Moon, D.; Lee, H.-J.; Lee, D.; Choi, D.; Bae, D.; Yuh, H.; Moon, Y.; Park, Y.; Yoon, E. Incorporation of Air-Cavity into Sapphire Substrate and Its Effect on GaN Growth and Optical Properties. *J. of Cryst. Growth* **2015,** *430*, 41-45.

Figure 1 (a) Amorphous Al_2O_3 on α-Al_2O_3. (b) Epitaxial γ-Al_2O_3 on α-Al_2O_3. (c) Epitaxial θ-Al_2O_3 on α-Al_2O_3. The unit cells of each polymorph appear as solid lines. (d) Reciprocal-space locations of x-ray reflections from α-Al_2O_3, γ-Al_2O_3, and θ-Al_2O_3 used in the experiments.

Figure 2 (a) Scattering geometry for x-ray experiments probing γ-Al_2O_3 400 and θ-Al_2O_3 600 reflections. The vectors X-ray k_{in} and X-ray k_{out} denote the directions and magnitudes of the wavevectors of the incident x-ray beam and the beam diffracted to the center of the detector, respectively. (b) Integrated intensities of θ-Al_2O_3 600 and γ-Al_2O_3 400 reflections obtained after heating to different temperatures. (c) Fractions of γ-Al_2O_3 and θ-Al_2O_3 as a function of heating temperature.

Figure 3 (a) Marginal and joint distribution of $\bar{q}_{6,Al-Al}$ and $\bar{q}_{6,O-O}$ from MD simulations of amorphous Al_2O_3, termed A in the legend, and the α-Al_2O_3, γ-Al_2O_3, and θ-Al_2O_3 polymorphs 1600 K and 1 atm. Atomic positions and the position dependence of $\bar{q}_{6,Al-Al}$ and $\bar{q}_{6,O-O}$ for (b) the amorphous Al_2O_3 on α-Al_2O_3 starting configuration and (c) the γ-Al_2O_3 on α-Al_2O_3 configuration reached after crystallization.

Figure 4 (a) Scattering geometry for x-ray experiments probing the $20\bar{2}$ and $40\bar{1}$ reflections of θ-Al_2O_3. Diffraction patterns exhibiting $20\bar{2}$ and $40\bar{1}$ reflections of θ-Al_2O_3 after heating to (b) 800 °C and (c) 1020 °C. (d) Intensities as a function of χ obtained by integrating across the indicated regions of (b) and (c). Notations A and B indicate which of two variants of θ-Al_2O_3 contributes to each reflection, such that $40\bar{1}$A and $20\bar{2}$A arise from variant A. The sharp features near χ=0 arise from scattering along the surface-normal reciprocal space truncation rod.

Figure 5 (a) θ/2θ x-ray diffraction scan along the surface normal direction of reciprocal apace after heating to 800 °C or 1020 °C for 1 hour. (b) Rocking curves of the γ-Al_2O_3 222 and θ-Al_2O_3 $40\bar{2}$

reflections for films heated to 800 °C and 1020 °C for 1 h.

Figure 6 (a) Scattering geometry for x-ray experiments probing γ-Al_2O_3 400 and θ-Al_2O_3 600 reflections. (b) X-ray diffraction pattern recorded using the geometry indicated in (a) during a rocking scan after heating to 800 °C. (c) Intensity as a function of 2θ obtained by integrating 2.5°-wide range of χ angles near the γ-Al_2O_3 400 reflection. (d) X-ray diffraction pattern recorded during a rocking scan after heating to 1020 °C. (e) Intensity as a function of 2θ obtained by integrating the same range as (c), exhibiting the γ-Al_2O_3 400 and θ-Al_2O_3 600 reflections.

Figure 7 Bonding configurations and epitaxial relationships at the interfaces of (a) epitaxial γ-Al_2O_3 on α-Al_2O_3, and (b) epitaxial θ-Al_2O_3 on α-Al_2O_3.

Figure 8 Representative structures of γ-Al_2O_3 in which (a) all Al vacancies occupy octahedral sites, (b) all Al vacancies occupy tetrahedral sites, and (c) the occupation has the same statistics as the site occupation matching the experimentally observed lattice parameter. The inset shows the local configuration of octahedral and tetrahedral Al sites.

Liu *et al.* Figure 1

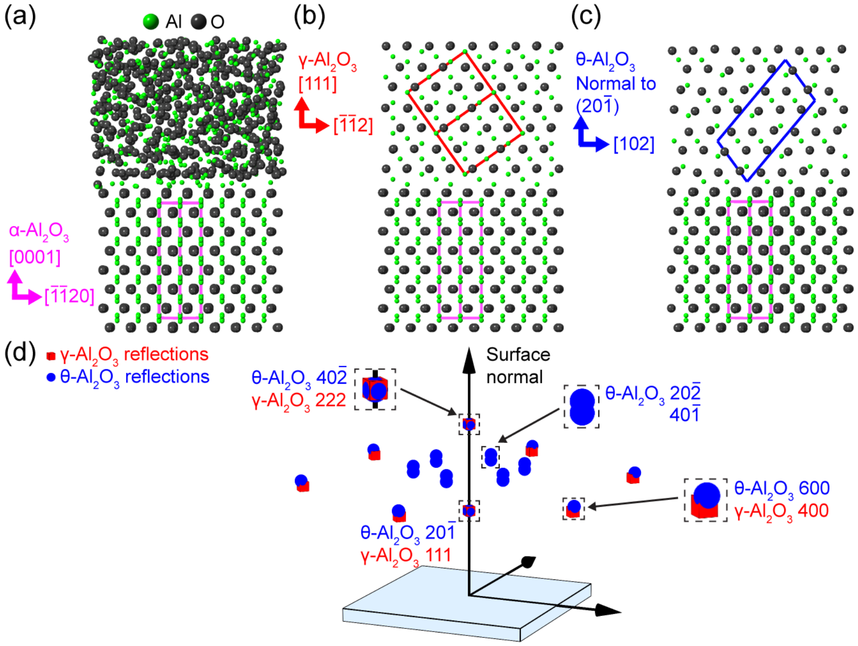

Liu *et al.* Figure 2

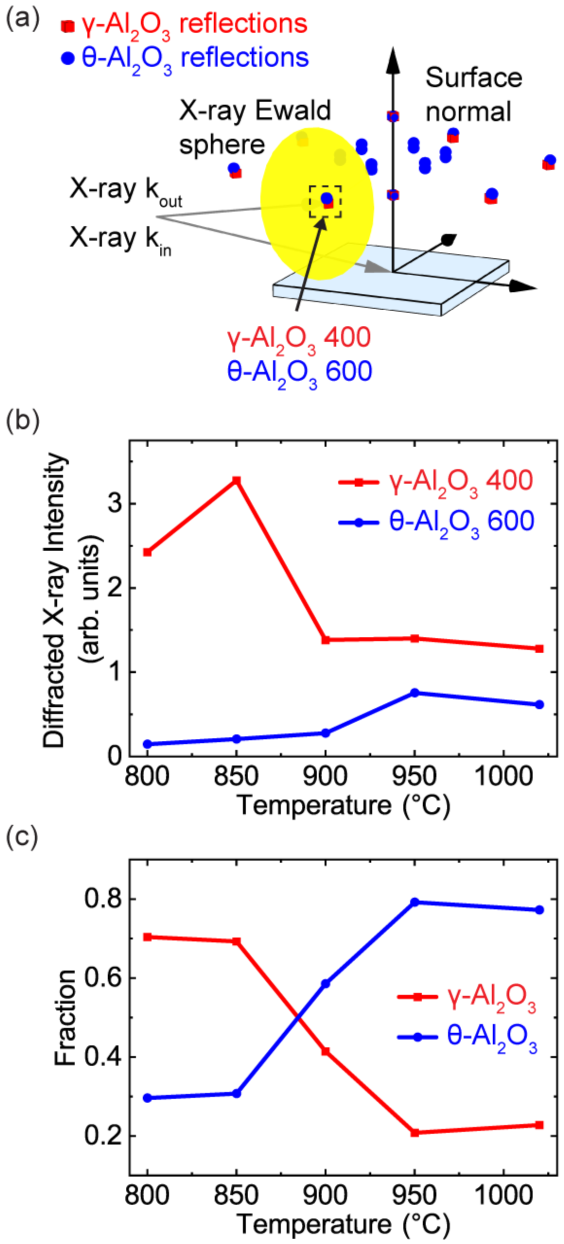

Liu *et al.* Figure 3

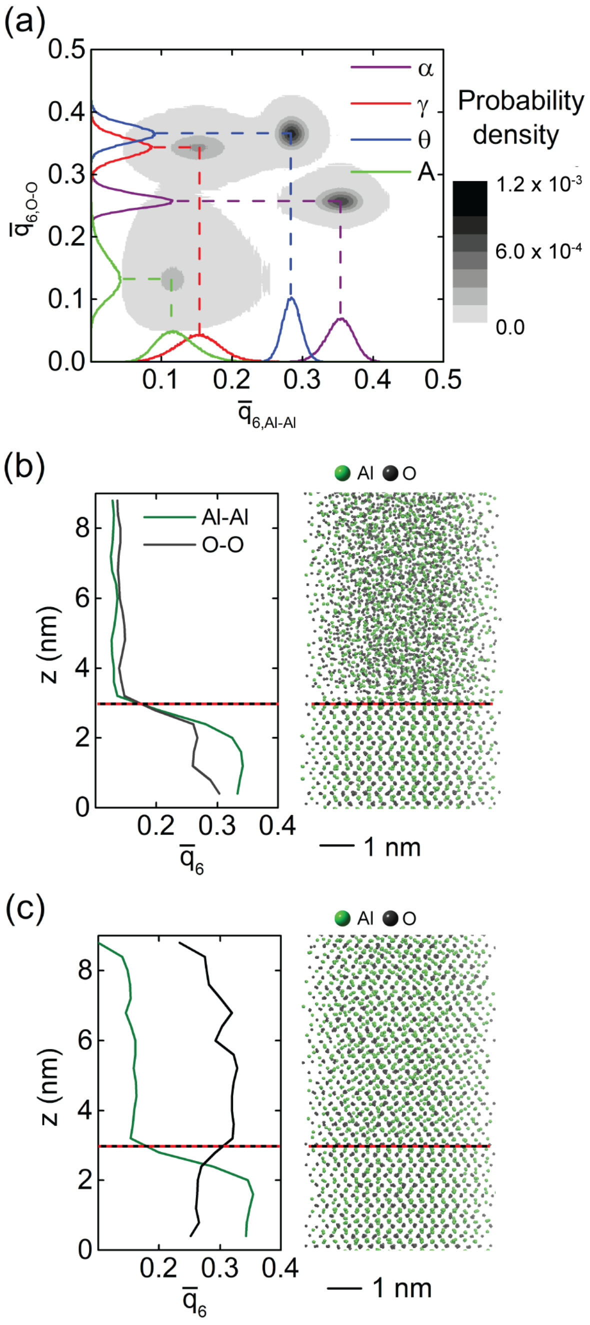

Liu *et al.* Figure 4

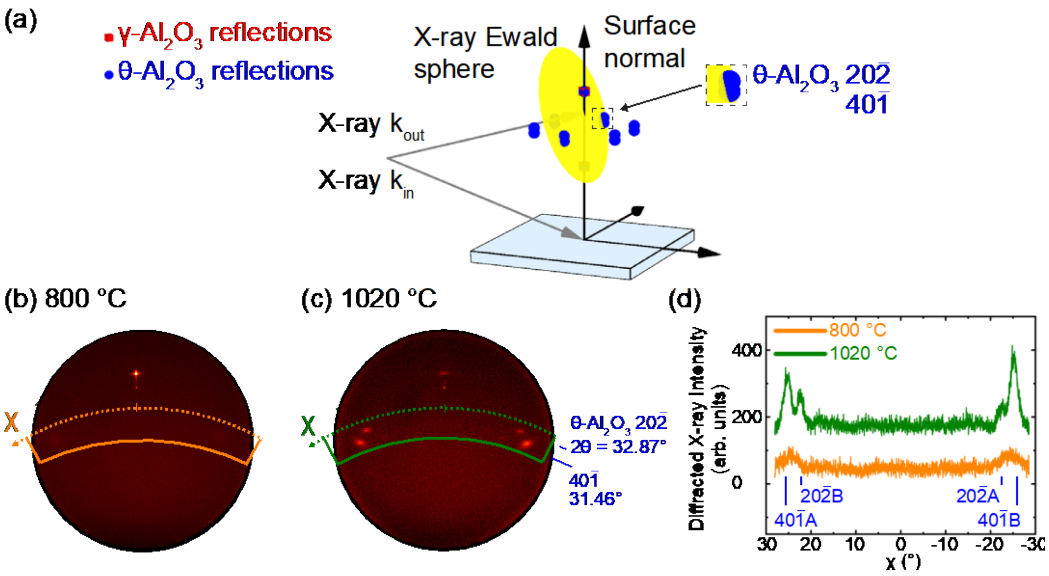

Liu *et al.* Figure 5

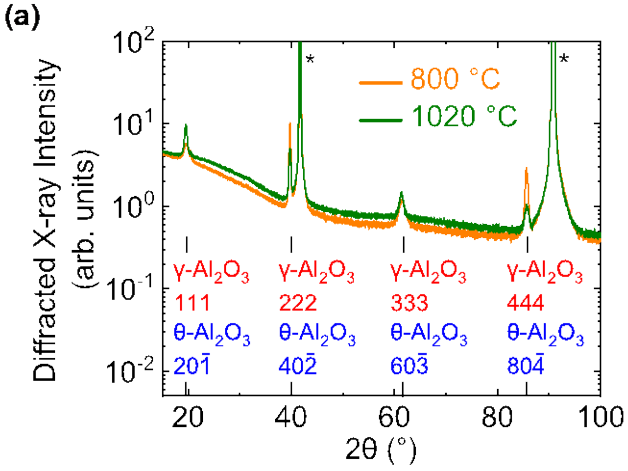

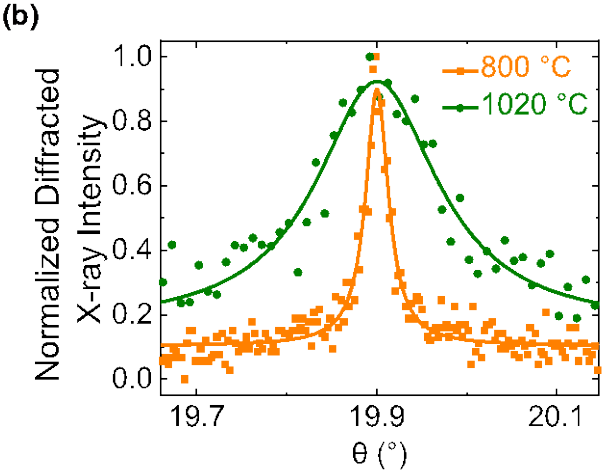

Liu *et al.* Figure 6

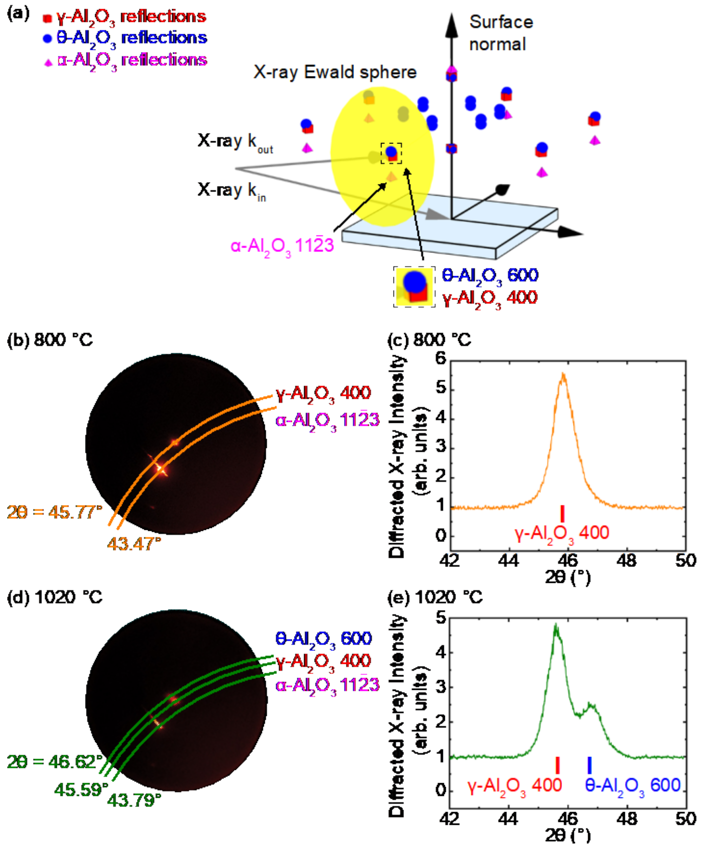

Liu *et al.* Figure 7

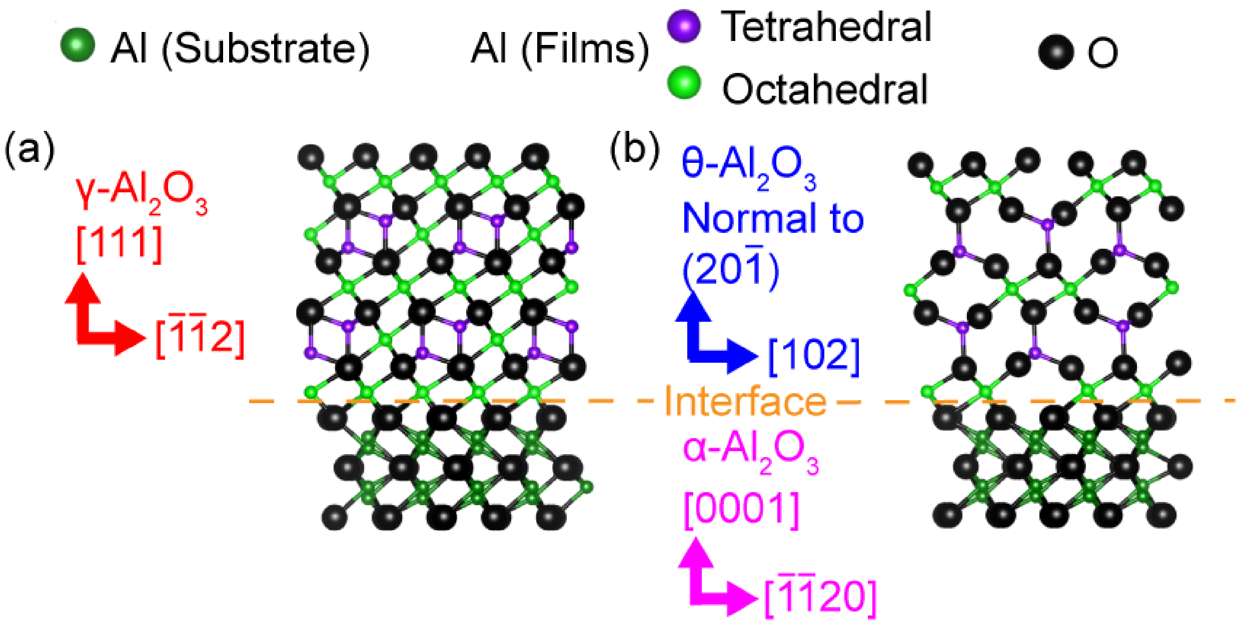

Liu *et al.* Figure 8

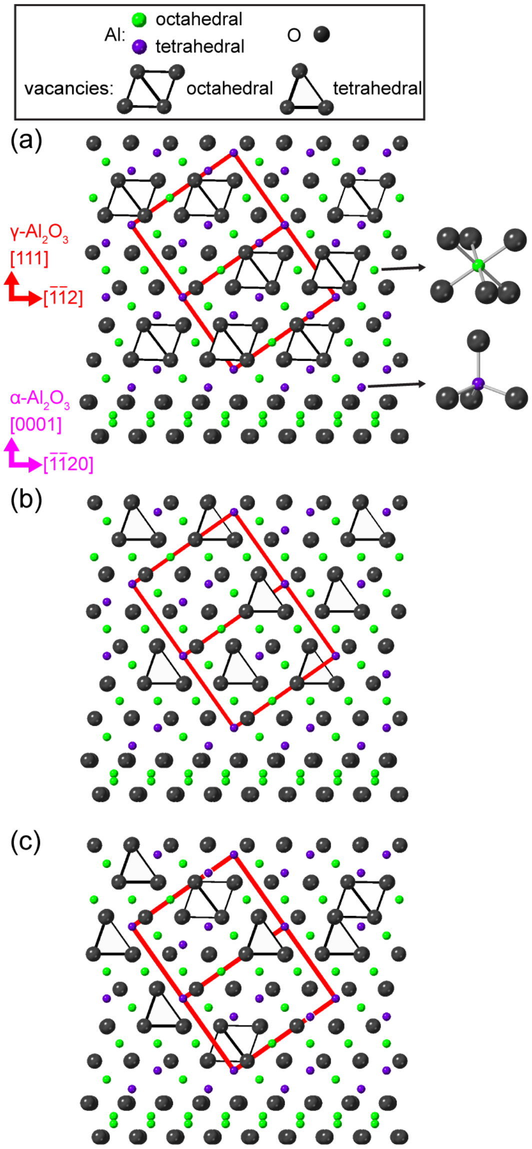

Liu *et al.* Table of Contents Graphic